

Chemical changes induced by ultrasound in iron

G. Albertini · V. Calbucci · F. Cardone · A. Petrucci ·
F. Ridolfi

Received: 22 May 2013 / Accepted: 18 July 2013 / Published online: 4 September 2013
© Springer-Verlag Berlin Heidelberg 2013

Abstract The focus of this work is a careful chemical investigation of structural damage produced by the exposure of an iron bar to pressure waves generated using an ultrasound machine (called the R-1-S reactor).

In addition to the emission of neutron bursts, the ultrasound treatment caused the appearance of zones of macroscopic damage (~ 1 mm in size) on the exterior of the bar. Reflected-light optical and environmental scanning electron microscopy (ESEM) has shown that these external damage zones are characterized by microcraters and are covered by a thin layer of cracked amorphous material. Under back scattered electron (BSE) observation, this material shows a lower brightness than the intact ferrite surface. In addition, a zone with a high density of deformed cavities (~ 1300 per mm^2) with irregular walls and a maximum size

of $10 \mu\text{m}$ was found inside the bar. These deformed microcavities are partially filled with a material composed of a chaotic assemblage of submicron-sized (most likely amorphous) particles.

A careful compositional investigation of the chaotic material inside the microcavities using the semi-quantitative data obtained with the ESEM X-ray Energy Dispersive System (EDS) has shown that it is primarily composed of carbon, manganese and chromium. These elements are also found in lower amounts within the intact ferrite matrix. In contrast, the damaged surface surrounding the craters is characterized by elements not found in the ferrite at all (i.e., O, Cl, K, Cu); elements the presence of which cannot be attributed to the occurrence of non-metallic inclusions or to contamination during fabrication.

These results are also difficult to explain using the generally accepted laws of physics; however, they do appear to agree with a recent theory predicting the deformation of the local spacetime and the violation of the Local Lorentz Invariance. Such a violation should occur following the collapse of micron-sized discontinuities internal to the materials (micropores) exposed to ultrasonic pressure waves resulting in an energy density to time ratio large enough to overcome the threshold predicted by the deformed space-time theory, triggering, in this way, a new kind of nuclear reaction. Following this theory, the C-, Mn- and Cr-rich chaotic material inside the microcavities is the product of the spherically symmetrical collapse of micropores internal to the ferrite while the presence of new elements within the cratered damage zones on the ferrite surface can be attributed to the catastrophic collapse of the subsurface pore walls resulting from microexplosions.

G. Albertini · V. Calbucci
Dipartimento di Scienze e Ingegneria della Materia dell'Ambiente
ed Urbanistica (SIMAU), Università Politecnica delle Marche
(UNIVPM), Via Brecce Bianche, 60131 Ancona, Italy

G. Albertini
CNISM (Consorzio Nazionale Interuniversitario per le Scienze
fisiche della Materia), Ancona Unit, Ancona, Italy

F. Cardone
Istituto per lo Studio dei Materiali Nanostrutturati (ISMN-CNR),
Via dei Taurini, 00185 Roma, Italy

F. Cardone · A. Petrucci
GNFM, Istituto Nazionale di Alta Matematica “F. Severi”, Città
Universitaria, P.le A. Moro 2, 00185 Roma, Italy

F. Ridolfi (✉)
Dipartimento di Scienze della Terra, della Vita e dell'Ambiente
(DiSTeVA), Università degli Studi di Urbino “Carlo Bo”, Campus
Scientifico “Enrico Mattei” Via Cà Le Suore 2, 61029 Urbino,
Italy
e-mail: filippo.ridolfi@uniurb.it

1 Introduction

Since 2009 various experiments have been performed on solid crystalline materials [e.g., 1–4] with the goal of verifying the theory predicting local space-time deformation [5, 6] and piezonuclear reactions (i.e., nuclear reactions induced by pressure), and confirming the results of ultrasound experiments in aqueous solutions [e.g., 7–9].

Recently, Cardone and collaborators have applied longitudinal ultrasonic waves and compression cycles to Fe–C alloys [3, 10]. Specifically, the application of ultrasound to cylindrical bars of steel and alpha-iron (ferrite) has resulted in the emission of neutron bursts and produced several roughly circular dark regions with diameters of a few millimeters on the bar surfaces [10]. Such clear evidence of reactions on the cylindrical bar surfaces is difficult to explain using traditional theoretical principles and leaves little room to doubt about the existence of a hereto unknown phenomenon triggered by pressure waves [11]. It was thus suggested that the damage on the surfaces of the steel and ferrite bars is the result of local piezonuclear reactions triggered by the sudden collapse of inter-crystalline cavities under the influence of extremely high local pressure produced by the ultrasound treatment [10, 11]. Ridolfi et al. [11] also found a zone with a high density of deformed microcavities partly filled with amorphous material within one of the ferrite bars treated with ultrasound in [10]. Preliminary X-ray atomic microanalyses of the external damage zones on the steel and iron bars have also shown the presence of elements absent in the undamaged zones [10]. However, Ridolfi et al. [11] have pointed out that the preliminary EDS microanalyses are not sufficient to confirm without a shadow of a doubt that the observed elements are the products of nuclear reactions since the Fe–C alloys are generally characterized by solid, non-metallic inclusions that could play a fundamental role in what happens during the ultrasound treatments.

This work is a follow-up of the preliminary results in [11] and primarily focuses on the microstructural and microchemical characterization of damage produced in a ferrite bar by the ultrasound treatment. Careful microstructural and semi-quantitative ESEM-EDS analyses of the surface and interior of the ultrasonically treated ferrite bar were performed to confirm the previous results and try to shed new light on the physical mechanism by which these reactions are induced. In particular, this work attempts to answer some questions that arose in a previous study [11] and to provide some physical parameters of the ferrite bar that should be taken into consideration in any further investigations and eventual application of the results.

2 Ultrasonic experiments

This section summarizes the primary characteristics of the ultrasonic machine used and briefly describes the setup of the ultrasound treatment [10].

The experiments were performed with a machine (i.e., R-1-S) that is similar to those used for treating aqueous solutions [e.g., 7, 8]. R-1-S was designed by Startec Ltd. together with one of the authors (FC) with the specific goal of treating cylindrical metal bars. The R-1-S machine has a converter unit with piezoelectric ceramics connected to a truncated conical sonotrode. A metallic frame holds the converter–sonotrode unit aligned with the cylindrical iron bar to be treated. The primary differences between this machine and those used to treat liquids [e.g., 7, 8] are a truncated conical reflector and the shape of the bar tips [10]. This allows the application of two trains of longitudinal ultrasonic waves of opposite direction parallel to the axis of the cylindrical bars [10] resulting in transverse compression of the bar. A patent on this experimental equipment is pending [12].

The sonotrode vibration amplitude used was 15 μm and all the steel and iron bars were exposed to ultrasonic waves with a power and a frequency of 19 W and 20 KHz, respectively. All the steel and iron bars were 20-cm-long cylinders with a diameter of 2 cm. Neutron burst emissions from the bars were registered within just 5 minutes of the beginning of the ultrasound treatment and continued for the rest of the experiment (1 hour). In addition, the ultrasonic treatment has resulted in the formation of several evident millimeter-sized structural damage zones on the circular surfaces of all the bars. These damage zones are distributed in an apparently random fashion on the external surfaces of the bars and are roughly circular in shape. See [10] for additional information on the experiments and their results.

3 Analytical methods

Even though the ultrasonic treatment of steel bars has produced a greater number of decidedly larger external damage zones with respect to those on the ferrite bars [10, 11], the ferrite represents an iron and carbon alloy with superior purity and with a decidedly inferior carbon content with respect to the steel. This makes any changes in the carbon content more evident. In addition, the ultrasound treated steel bars have previously undergone external hardening [10]. This hardening results in chemical heterogeneities on the surface of the steel bar that could be difficult to distinguish from the products of reactions responsible for structural damage. Consequently, it has been decided that one of the ferrite (i.e., alpha iron) bars, and not the steel, should be the focus of a detailed characterization.

The ferrite bar and the samples extracted from it have been furnished by Walter Sala (Startec Ltd.'s administra-

tor) and were independently analyzed in 2011 and 2012 at the laboratories of the Università di Urbino “Carlo Bo” (hereafter UNIURB) and of the Università Politecnica delle Marche (UNIVPM). Sample preparation was begun by Startec Ltd. and consisted of radial extraction of two parallelepipeds from the cylindrical ferrite bar using a wire-EDM (Electric Discharge Machining). The long dimensions of the parallelepipeds correspond to the bar diameter (20 mm) and the square, curved bases have an area of $\sim 4 \text{ mm}^2$. The base of the first parallelepiped contains one of the dark damaged areas (Figs. 1a, b) whereas the second sample was extracted from an undamaged zone of the bar surface [11].

A first series of analyses of the square bases of the two parallelepipeds representing the external curved surface of the bar were performed using optic microscopes and an Environmental Scanning Electron Microscope (ESEM) of UNIURB. After these analyses, the samples were prepared for investigation of the internal zones of the bar at UNIURB. One of the long faces of each of the parallelepipeds was polished using sandpaper and diamond paste of various grit sizes (9, 6, 3, 1 μm). In order to obtain a cross-sectional view, the sample was polished down to the center of the external damage zone. The polished surfaces were immediately (≤ 10 seconds) cleaned with water and 90 % ethyl alcohol and dried using compressed air. The polishing, cleaning and drying procedure took approximately 10–15 minutes to complete (see [11] for additional information).

Preliminary characterization of the samples was done using optic microscopy. Most of the ESEM analyses were performed with a FEI Quanta 200 at UNIURB, which is equipped with a field emission gun, secondary electron (SE) and back scattered electron (BSE) detectors, and an Energy Dispersive System (EDS) for X-ray atomic analysis. The ESEM operational conditions were a vacuum of 5.0×10^{-6} mbar, an accelerating voltage of 30 kV, and a beam current of 264 mA. All the in situ X-ray analyses were performed with a counting time of 100 seconds and maintaining a working distance of 9.7 mm. This setting allows to identify almost all the natural elements of the periodic table (from B to U) and allows for maximum SE and BSE image resolutions of 3.0 and 4.0 nm, respectively. The qualitative results obtained with the ESEM-EDS [11] were counterchecked using the FESEM ZEISS SUPRA 40 at UNIVPM.

In order to obtain quantitative data using the ESEM-EDS at UNIURB, the energy-dispersive spectra are generally processed using the electron microscope analytical software. However, we found that the software corrections resulted in a large carbon overestimation such that the ferrite and steel showed steel and cast iron compositions, respectively. To avoid this processing glitch, quantitative data were obtained by calculating the proportions of the net areas under element peaks corrected for standard peak intensities. All the EDS spectra were carefully checked for artifacts

such as escape peaks, sum peaks and peak overlaps. We identified two artifact peaks with energies comparable to the $\text{K}\alpha_{1,2}$ peak of Si and the $\text{La}_{1,2}$ peak of La which are due to the high Fe count rate. The counts at the La $\text{La}_{1,2}$ peaks were discarded whereas the average ratio between the net area under the Si $\text{K}\alpha$ artifact peak and that of the Fe $\text{K}\alpha$ peak for the intact ferrite ($f = \frac{\text{Si K}\alpha}{\text{Fe K}\alpha} = 3 \times 10^{-3}$, $\sigma = 7 \times 10^{-4}$) was used to roughly estimate the effective net area due to Si $\text{K}\alpha_{1,2}$ in the damaged zones: $\text{Si K}\alpha_{\text{effective}}^i = \text{Si K}\alpha_{\text{measured}}^i - f \cdot \text{Fe K}\alpha_{\text{measured}}^i$.

In general, the percent error of the X-ray microanalyses is inversely correlated with the content of the analyzed element [e.g., 13]. However, the compositional data presented in this work must be considered semi-quantitative as no standards were used to calibrate the X-ray element peaks (i.e., no information on accuracy is available).

4 Results

4.1 Structural analysis

Microscope and ESEM observations allowed us to obtain microstructural data of the external damage and the interior of the ferrite bar (Figs. 1, 2). The predominantly black damage mark on the ferrite surface is mostly irregular in shape and well distinguishable from oxidized (rust) patches and the drawn, intact surface of the ferrite bar (Fig. 1a). It is worth noting that the rust patches were not present at the time of the ultrasound treatment (2009) and are most likely the result of natural oxidation of the iron on the ferrite surface between 2009 and 2011.

BSE imaging of the damage mark shows a cratered surface of lower brightness (i.e., low average atomic weight) with respect to the intact ferrite surface (Figs. 1b, c). Bright remnants of the original ferrite surface can also be found between the cratered zones, which are characterized by irregular and cracked interiors composed of a material with a lower mass (i.e., dark) (Figs. 1c–e). The cross-sectional view of the damage mark indicates that the thickness of the low-brightness material is minimal, possibly ≤ 1 micron (Fig. 1f). The deeper craters have depths up to 20 μm and, together with the bright remnants of intact ferrite, suggest that highly energetic microexplosions occurred (Figs. 1e, f).

The internal structure of the bar appears mostly uniform with occasional defects in the form of roundish microcavities (Fig. 1f). However, a zone of $\sim 0.5 \text{ mm}^2$ with a large number of microcavities ($\sim 1.3 \times 10^3$ per mm^2) was found at a distance of ~ 0.3 mm from the external damage mark (Fig. 2a). The largest of these cavities has a diameter of $\sim 10 \mu\text{m}$. At higher magnifications the cavities appear highly deformed with irregular contours and are partially filled with chaotic, amorphous material (Figs. 2b, c). The hypothesis that this material is the remnant of the oil-based diamond pastes used in sample preparation can be safely discarded as

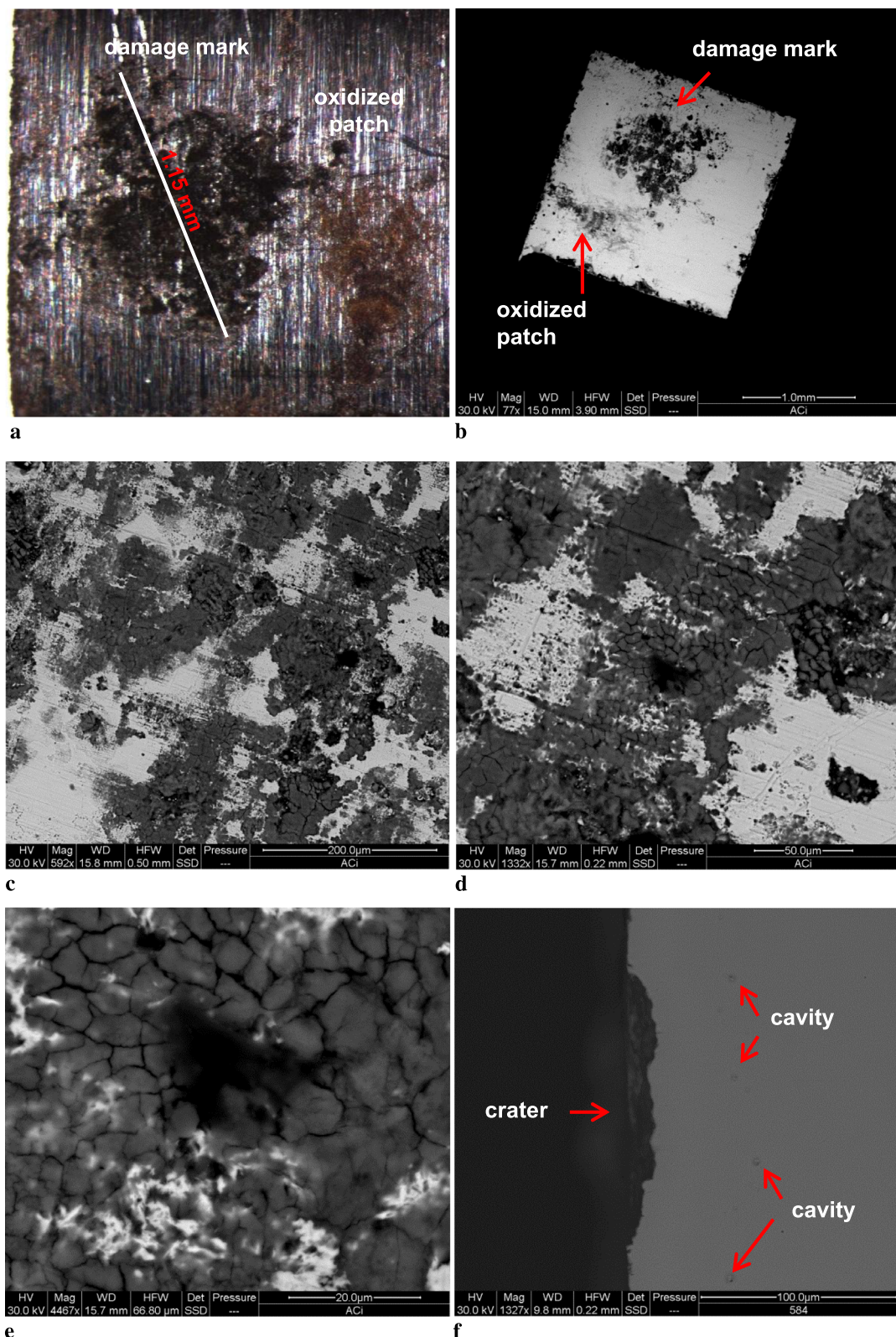


Fig. 1 Microphotograph (a) and BSE images (b)–(f) of the parallelepiped with the damage mark. (a) and (b) show panoramic views of the damaged surface; an oxidized patch next to the *damage mark* is also shown. (c) and (d) are close-up views of the damage mark. (e) is

an enlargement of (d) showing a deep crater surrounded by a dark and cracked surface. (f) is a cross-sectional view of the damage mark; the occurrence of small cavities is also shown (modified after [11])

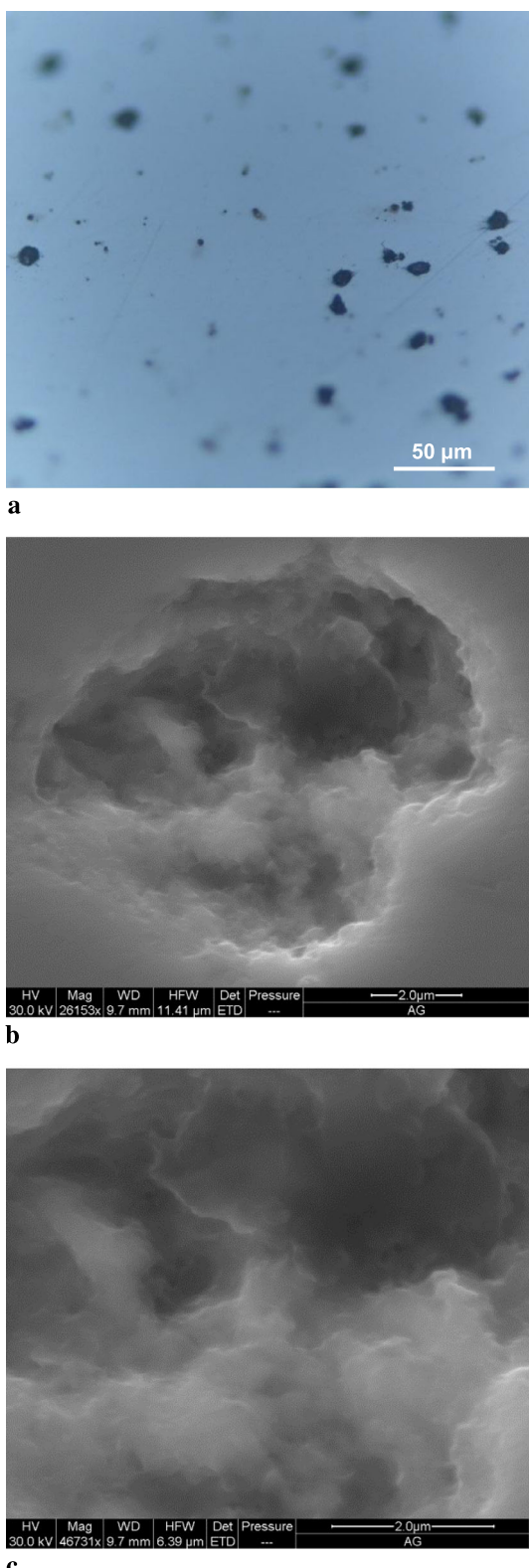


Fig. 2 Microscope polarized light (**a**) and SE images (**b**)–(**c**) showing a microcavity-rich zone inside the bar (**a**) and the microstructure of one of these cavities (**b**). (**c**) is a close-up view of the cavity interior in (**b**) (modified after [11])

the amorphous material does not show any diamond grains or blurring typical of fatty materials observed under SE. In addition, this material appears stable under the heating effect of the focused electron beam.

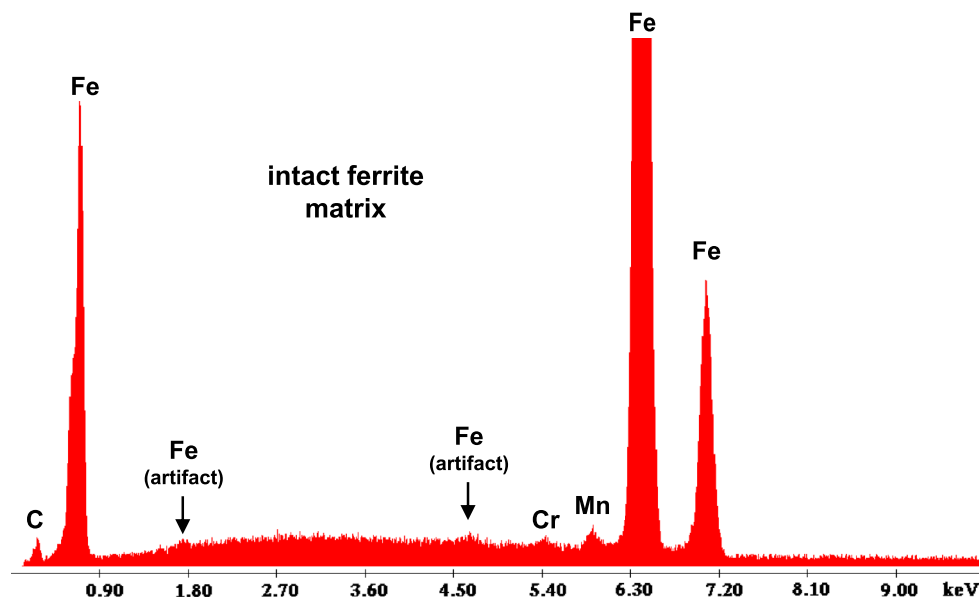
It is worth noting that neither the external damage zones nor the areas characterized by a high density of microcavities filled with amorphous material were found on either the external surface or the interiors of the reference parallelepiped, which did occasionally show smaller sized ($<5\text{ }\mu\text{m}$) empty cavities. Some typical Fe–C alloy inclusions (see Ref. [14]) found in both samples are Mg and Ca spinels and oldhamite: a CaS phase with minor Mn, Mg and C contents. These non-metallic phases are not abundant and do not show evidence of any type of reaction. They are usually found as small ($\leq 2\text{ }\mu\text{m}$) sub-euhedral inclusions in the ferrite matrix. In addition, it is important to note that the area characterized by a high density of deformed microcavities filled with amorphous materials was identified during the initial polishing of the sample in correspondence with the damage mark center. The three successive attempts to locate other zones with similar densities of microcavities or isolated microcavities filled with amorphous materials through further removal of ~ 20 – $40\text{ }\mu\text{m}$ of material from the ferrite parallelepiped with the damage mark were not successful. However, one elongate and irregular cavity (maximum dimension $\sim 15\text{ }\mu\text{m}$) hosting several small crystals of Mg–Ca spinel [i.e., $(\text{Mg}, \text{Ca})\text{Al}_2\text{O}_4$] was found. Although these small spinels were potentially surrounded by gas, similarly to oldhamite inclusions, they did not show any type of reaction.

4.2 EDS spectra and data

Preliminary EDS analyses of the ferrite matrix and the anomalous structural features found in the parallelepipeds were performed [11]. Figure 3 shows a reference spectrum of the homogeneous intact ferrite while Fig. 4 reports two representative X-ray spectra of materials on the external damage mark and inside the microcavities. The ferrite matrix, as expected, is composed of iron with minor amounts of carbon, chromium and manganese. The intact ferrite spectrum also shows two artifact peaks with energies matching the $\text{Si K}\alpha_{1,2}$ and the $\text{La L}\alpha_{1,2}$ peak, a consequence of the high Fe count rate.

These peaks, as well as those characteristic of Fe, C, Cr and Mn, can also be found in the spectra of the external damaged zone and of the microcavities in the bar. In addition, the spectra of the damage mark (e.g., Fig. 1c) show peaks of elements not present in the intact ferrite such as oxygen, sodium, aluminum, sulfur, chlorine, potassium, calcium and copper, as well as a more pronounced carbon peak (e.g., Fig. 4). This enrichment in carbon is particularly evident in the spectra of the formless material filling the microcavities (Figs. 2c, d), which is also characterized by lower

Fig. 3 Qualitative EDS spectrum of the polished surface of the reference ferrite parallelepiped. (Reprinted with permission from Ref. [11], Ridolfi F., Cardone F., Albertini G. Ultrasonic Damage in Iron, Journal of Advanced Physics, 2013, Vol. 2, 40–44, doi:10.1166/jap.2013.1045. Copyright © American Scientific Publishers)



amounts of oxygen and sulfur with respect to the damage mark (Fig. 4).

Semi-quantitative EDS data of the anomalous materials on the surface and inside the bar are shown in Tables 1 and 2 together with the average composition and the standard deviation (σ) of 12 external and internal analyses of the intact ferrite. The lower amount of data for the amorphous material inside the microcavities (Table 2) is due to the difficulties inherent in the analyses of chaotic material inside the microcavities. Indeed, several microanalyses of this material had to be discarded due to low number of X-rays detected (expressed as counts s^{-1}).

The composition of the intact ferrite is fairly homogeneous. Besides iron (Fe = 98.5 wt.%), small amounts of carbon (C \leq 0.1 wt.%), chromium (Cr = 0.4 wt.%) and manganese (Mn = 1.0 wt.%) were detected in the intact ferrite. The σ values indicate a high overall precision with relative uncertainties that increase from iron (0.1 %) to carbon (21 %), i.e., with decreasing contents of the analyzed element (e.g., Table 1).

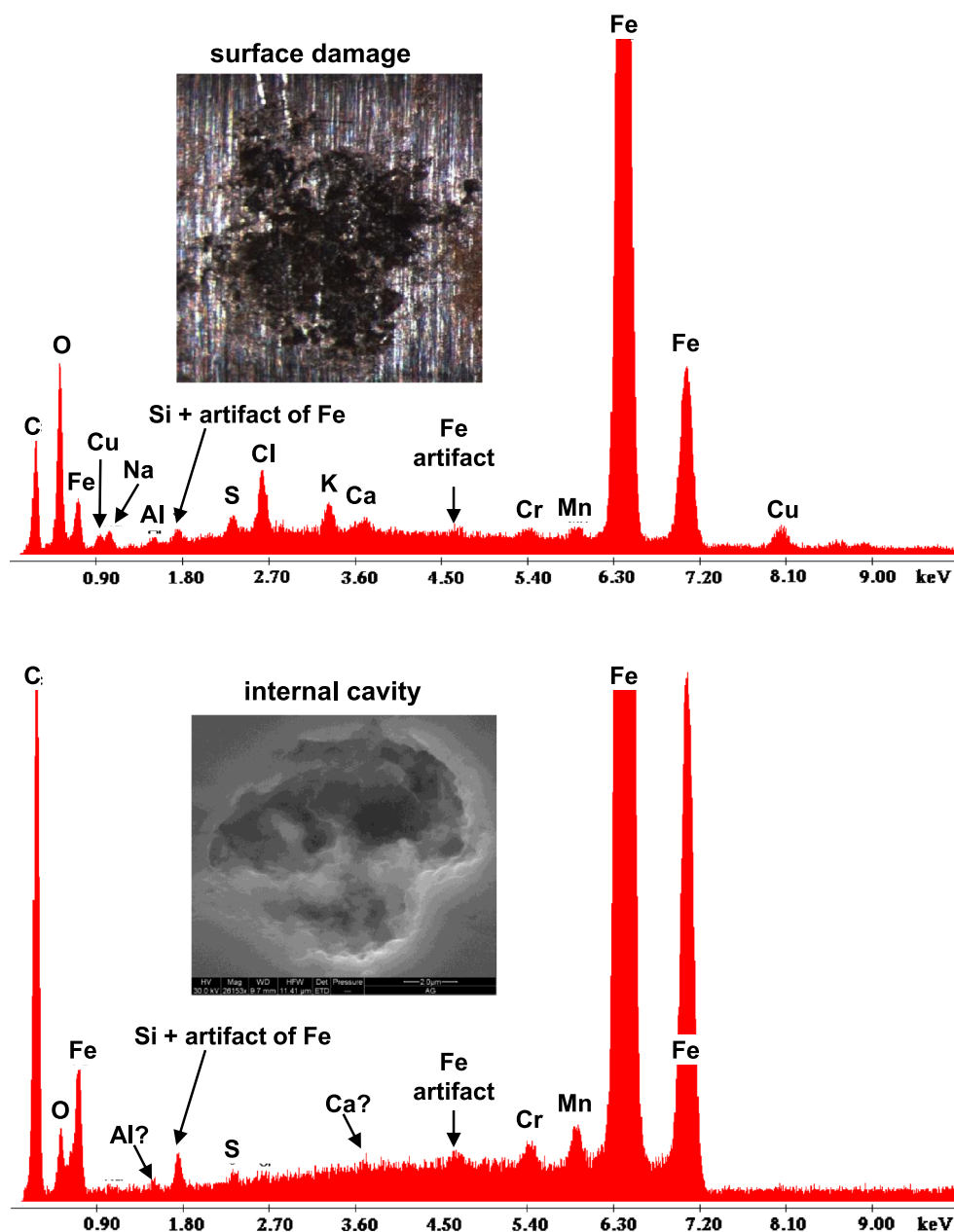
The low-brightness material in the external damage zone (Fig. 1c) shows variable compositions characterized by lower Fe (83.4–90.0 wt.%) and Mn (0.5–0.9 wt.%) contents and higher C and Cr values (0.2–1.4 and 0.4–2.0 wt.%, respectively) than the intact ferrite. In addition, the damage mark shows remarkable and variable amounts of elements foreign to the matrix of the intact ferrite, such as oxygen (O = 2.2–6.9 wt.%), chlorine (Cl = 1.5–2.9 wt.%), potassium (K = 0.9–1.4 wt.%) and copper (Cu = 0.7–3.8 wt.%), as well as smaller concentrations of sodium, silicon and sulfur (\leq 0.6 wt.%). Small amounts (\leq 1.0 wt.%) of magnesium, aluminum and calcium are found only occasionally (Table 1).

The X-ray microanalyses of the jagged material inside the microcavities of the bar interiors show a lower number of foreign elements (Table 2). Na, Mg, Cl, K and Cu are apparently missing and the concentrations of Al, Si, S and Ca are vanishingly small (\leq 0.2 wt.%). The contents of iron and oxygen measured in these small cavities (94.3–98.2 and 0.0–1.2 wt.%, respectively) are intermediate between those of the damage mark and the intact ferrite but closer to the ferrite composition. Astonishingly, the analyses of the microcavity material systematically show higher C, Cr and Mn concentrations than the intact ferrite (Table 2). The exsolution (i.e., remobilization in the solid state) of these elements during the ultrasound treatment appears to be rather improbable since the material within the microcavities should have been associated with components poor in these elements and rich in Fe with respect to the ferrite.

4.3 Data processing and interpretation

The structural characteristics of the damage mark and the material composing it (Fig. 1) suggest that it is the result of violent reactions within subsurface zones, which possibly have led to the partial fusion of the ferrite and the sudden fracturing and expulsion of the superficial layers of the bar. This is supported by the presence of bright remnants of pristine ferrite surface between the cratered dark material (Figs. 1c, d) and by the limited depth (\sim 20 μ m) of the craters (Figs. 1e, f). In addition, the cracking of the cratered material (Fig. 1e) suggests that the material generated by the reaction was liquid and interacted with the surrounding atmosphere cooling rapidly. Furthermore, parts of the fused material were most likely expelled during the explosive phase as suggested by its minimal thickness in cross-sectional view (Fig. 1f). This is in agreement with the presence of characteristic ferrite peaks (i.e., those of Fe, Cr, Mn) in the EDS

Fig. 4 Qualitative EDS spectra of the surface damage mark and of the amorphous material inside an internal cavity of the ferrite bar. The two spectra were obtained at the same operating conditions and have the same vertical counting scale. (Reprinted with permission from Ref. [11], Ridolfi F., Cardone F., Albertini G. Ultrasonic Damage in Iron, Journal of Advanced Physics, 2013, Vol. 2, doi:10.1166/jap.2013.1045. Copyright © American Scientific Publishers)



spectra of the damage mark (Fig. 4) which suggest that the ESEM electron beam had penetrated the entire thickness of the damaged material and was interacting primarily with the ferrite matrix (see Fig. 3 for reference spectrum).

The irregular morphology of the material inside the microcavities (Figs. 2b, c) cannot be an artifact of the low resolution of the ESEM because, at the operating conditions used, the FEI Quanta 200 is capable of distinguishing objects with dimensions of as little as 3 nm. It is therefore safe to assume that the material inside the microcavities is composed of a chaotic assemblage of submicron-sized, likely amorphous particles. The EDS spectra of the material in the microcavities (e.g., Fig. 4) are inferred to be the result of the summation of X-rays originating from the materials within

the microcavities (to a small degree) and those of the ferrite matrix underneath (to a large degree) just as for the damage mark. The second spectrum in Fig. 4 shows that the material inside the microcavities is predominantly composed of carbon.

All of this indicates that the amount of material foreign to the ferrite is minimal. This is supported by the relatively high Fe contents in all the spot analyses of the external damage mark (Table 1) which is in contrast with the low BSE brightness of the material (e.g., Fig. 1c). Indeed, while back scattered electrons come from relatively shallow levels of the analyzed materials, the emitted X-rays derive from a bulb-shaped volume extending deeper into the sample. Even though the diameter of the ESEM electron beam

Table 1 ESEM-EDS semi-quantitative data (in weight %) of the amorphous material in the external damage zone. The average composition and standard deviation (σ) of 12 analyses of the intact ferrite

(including both external and internal zones) is also reported. n.m. = identified but not measured. Blank cells indicate that the element was not detected

Spot	Intact ferrite		External damage material												
	Average	σ (12)	ED1	ED2	ED3	ED4	ED5	ED6	ED7	ED8	ED9	ED10	ED11	ED12	ED13
C	0.08	0.02	0.40	0.24	0.23	0.33	0.21	0.37	0.26	0.57	0.75	0.67	1.37	1.10	1.05
O			4.27	5.86	5.84	6.13	6.91	6.85	6.58	4.14	3.31	2.19	2.81	3.26	3.88
Na			0.08	0.12	0.13	0.19	0.10	0.19	0.14	0.24	0.21	0.22	0.07	0.10	0.18
Mg										0.20	0.01				0.10
A1								0.14			0.10				
Si			0.09	0.21	0.07	0.17	0.16	0.13	0.12	0.29	0.09	0.36	0.23	0.30	
S			0.48	0.41	0.46	0.59	0.51	n.m.	n.m.	0.57	0.54	0.49	0.25	0.25	0.36
C1			1.76	2.80	2.86	2.75	2.74	2.71	2.70	2.20	1.98	1.75	1.62	1.53	1.48
K			0.99	1.17	1.38	1.09	1.29	1.27	1.20	1.07	1.07	1.06	1.16	0.99	0.87
Ca			0.46							0.99	0.48	0.25	0.22	0.22	
Cr	0.43	0.05	0.41	1.84	1.82	0.97	2.04	1.79	1.69	0.71	0.71	0.62	0.79	0.48	0.61
Mn	0.97	0.08	0.66	0.78	0.70	0.60	0.65	0.57	0.71	0.66	0.64	0.91	0.48	0.55	0.57
Fe	98.52	0.11	89.74	84.81	84.32	83.43	83.62	83.45	83.54	86.85	87.21	89.82	89.75	90.05	89.05
Cu			0.75	1.88	2.05	3.84	1.76	2.66	2.92	2.86	2.11	1.59	1.09	1.23	1.33

Table 2 ESEM-EDS semi-quantitative data (in weight %) of the amorphous material inside the microcavities. The average composition and standard deviation (σ) of 12 analyses of the intact ferrite (including both external and internal zones) is also reported. Blank cells indicate that the element was not detected

Spot	Intact ferrite		Internal damage material						
	Average	σ (12)	MC1	MC2	MC3	MC4	MC5	MC6	MC7
C	0.08	0.02	0.25	0.67	0.49	0.90	1.40	0.65	2.93
O				0.82	0.88	1.20	0.33	0.40	0.35
A1						0.08			
Si			0.11	0.15	0.21	0.16	0.12	0.07	
S						0.08	0.14		
Ca						0.18			
Cr	0.43	0.05	0.47	0.51	0.47	0.68	0.68	0.91	1.00
Mn	0.97	0.08	1.02	1.14	1.12	1.10	1.25	1.10	1.43
Fe	98.52	0.11	98.15	96.71	96.83	95.95	96.05	96.56	94.29

is $\leq 0.5 \mu\text{m}$, its penetration depth and the extent of its interaction with the sample depends on the voltage used and the nature of the material being analyzed. For example, the Kanaya–Okayama formula [15] which takes into consideration the ESEM beam energy (i.e., 30 kV) and the physical properties of the analyzed material, gives beam penetration depths of 3.2 and 9.9 μm for ferrite and amorphous carbon materials, respectively. This indicates that most of the measured X-rays come from the ferrite lattice below the damage mark and microcavity materials. Therefore, the material of the external damage mark should have a greater thickness than the materials in the microcavities, because it shows lower Fe contents. Using a simple mass balance equation that takes into consideration the composition of the underlying ferrite matrix, we have estimated that during the ESEM-EDS analysis of the external damage mark and the inter-

nal microcavities the electron beam interacted with materials containing 8.8–15.6 % and 0.4–4.3 % of mass foreign to the ferrite, respectively.

The fact that the data in Tables 1 and 2 are a product of the interaction of the electron beam with a combination of reaction products and the underlying ferrite matrix is of fundamental importance. In fact, plotting these data on element-to-element variation diagrams can give additional information about the effective composition and/or compositional variation of the analyzed material. For example, if the amorphous materials were as homogeneous as the ferrite, the data points would behave like an ideal mixing system in a Cartesian element-to-element variation diagram aligning along a straight line [e.g., 16]. This straight line should have a slope characteristic of the amorphous material and converge towards the ferrite composition. This ideal behavior becomes

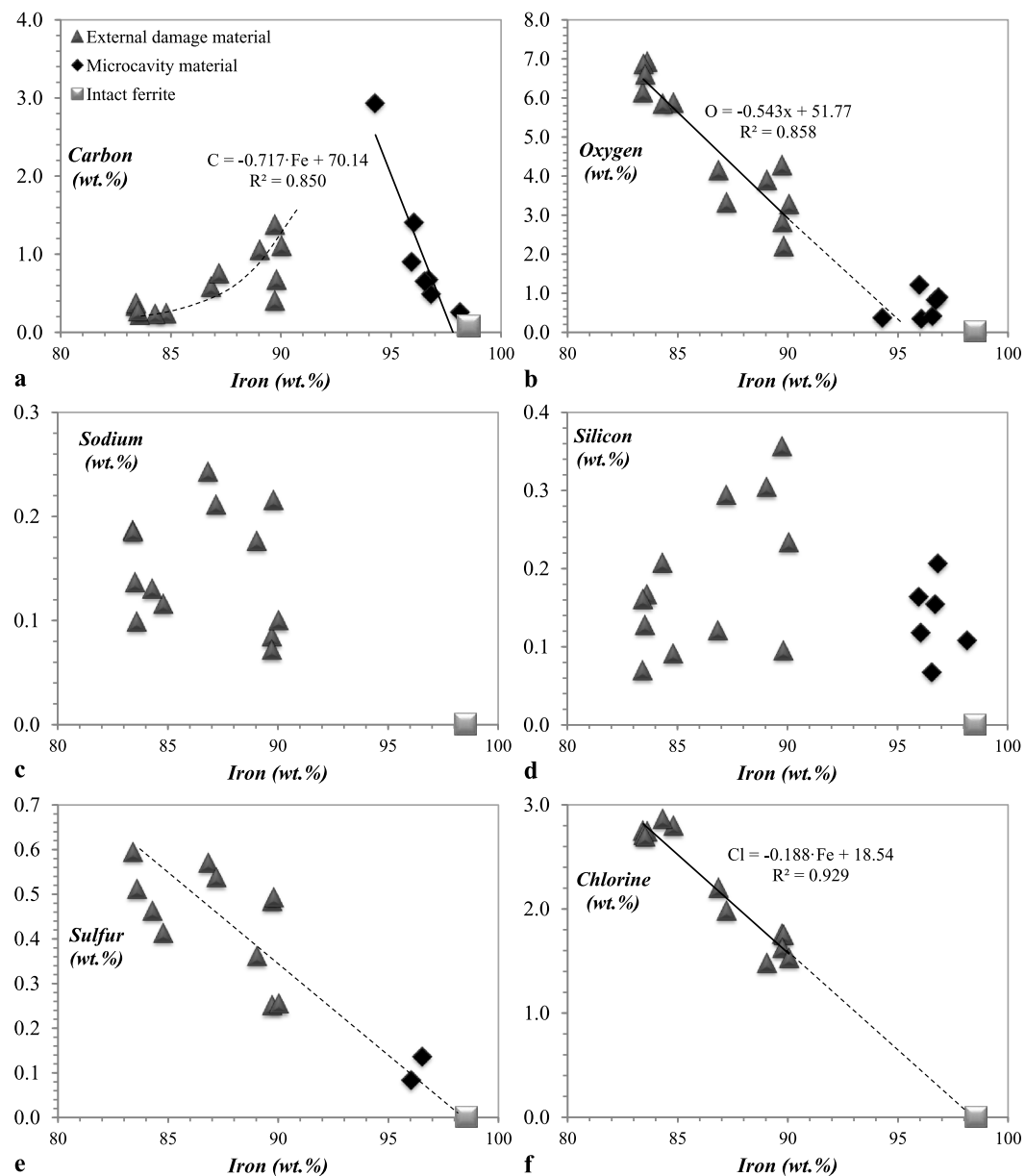


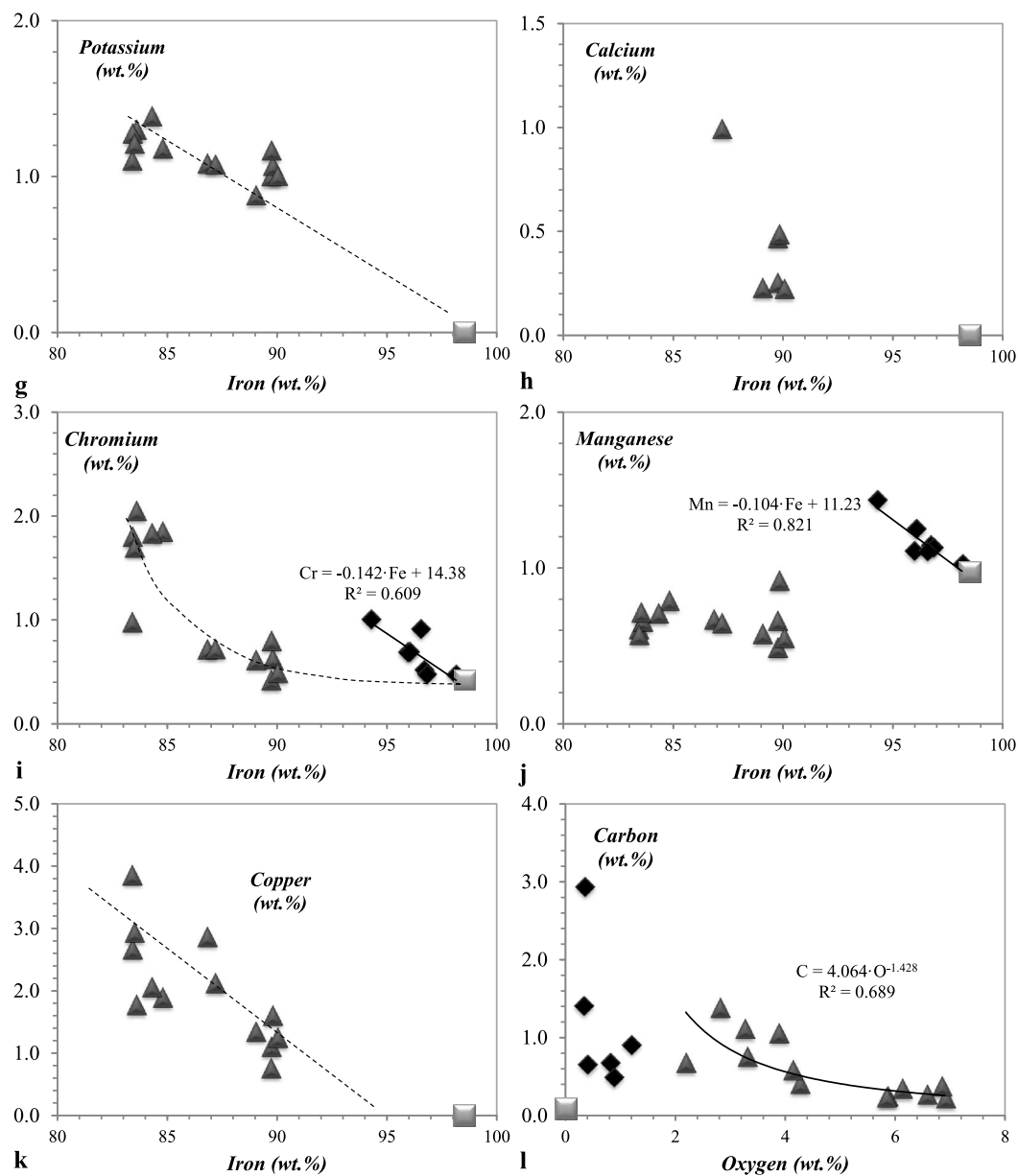
Fig. 5 Variation diagrams of (a) carbon, (b) oxygen, (c) sodium, (d) silicon, (e) sulfur, (f) chlorine, (g) potassium, (h) calcium, (i) chromium, (j) manganese and (k) copper with iron for the external damage and microcavities inside the bar; (l) is the carbon vs. oxygen diagram. The composition of the intact ferrite is shown in all the dia-

grams (data from Tables 1 and 2). The equations of linear regression (*solid lines*) with reasonably high determination coefficients (R^2) are also reported. Approximate correlations and extension of the solid lines to the composition of the intact ferrite are indicated by *broken lines* or curves

more obvious with increasing precision which is a function of the amount of material analyzed [e.g., 13, 17] and is influenced by the possible presence of unanalyzed elements with atomic numbers below that of boron. Any melting and/or mixing of the ferrite with the amorphous material, obviously, should not affect this behavior (e.g., He; [3, 10]). On the other hand, if the amorphous material were highly heterogeneous, because of, for example, contamination, the compositional data in Tables 1 and 2 would show no obvious correlations in element versus element diagrams. To

conclude, if the analyzed material were formed as a result of two or more different events, element versus element diagrams of the data would very likely display curvilinear patterns [e.g., 16].

In diagrams in Fig. 5, the Fe concentrations are compared with those of other elements from Tables 1 and 2. Because the amounts of Mg and Al detected in some of the damage mark analyses (Table 1) were extremely low and could thus represent slight environmental contamination, Fe versus Mg and Al plots are not shown.

**Fig. 5** (Continued)

Analyses of the external cratered zone show good linear correlations in Fe–O and Fe–Cl diagrams (R^2 of 0.86 and 0.93, respectively) that converge towards the ferrite composition (Figs. 5b, f). The slopes of these lines should be proportional to the contents of the plotted elements in the amorphous material; however, because the plotted data is based on semi-quantitative analyses (i.e. the accuracy of the data is not known), it is not possible to draw any meaningful quantitative conclusions. In fact, the slope of the line in Fig. 5b (i.e., 0.54) is consistent with an oxygen content (~ 54 wt.%) that is difficult to explain within a solid material such as the amorphous crust of the cratered damage zone. Inverse linear relationships, such as those shown by O–Fe and Cl–Fe, are

also present in S, K and Cu versus Fe diagrams (Figs. 5e, g, and k). Therefore, these elements (i.e., O, Cl, S, K, Cu) are the primary constituents of the amorphous material, while no meaningful conclusions can be drawn about the presence of Na and Si due to their low concentrations (≤ 0.4 wt.%; Figs. 5c, d; Table 1). Similarly to Mg and Al, calcium is occasionally detected in very small amounts, possibly due to environmental contamination. The manganese amounts are consistently lower than in the undamaged ferrite and it is very likely that, similarly to Fe, it is either absent in the material of the external damage zone or its presence is due to mixing with ferrite melted during the reaction (Fig. 5j). Chromium shows an anomalous behavior plotting in an ap-

proximately curvilinear pattern that points towards the ferrite composition (Fig. 5i). Equally surprising is the carbon behavior, which shows a non-linear pattern and instead of converging towards the ferrite composition appears to converge towards the maximum composition measured for the amorphous material inside the microcavities (Fig. 5a).

In fact, in a C–Fe diagram the analyses of the latter material show a highly linear behavior ($R^2 = 0.85$) which converges towards elevated carbon contents (Fig. 5a). In addition to carbon, the material inside the microcavities is composed predominantly of chromium and manganese as shown by their respective linear regression models (R^2 of 0.61 and 0.82; Figs. 5i, j). Oxygen is present in relatively small amounts (<1.2 wt.%; Fig. 5b; Table 2) and its presence is possibly due to oxidation during the relatively long (10–15 minutes) sample polishing process.

Silicon in the external and internal amorphous material is present in amounts (≤ 0.4 wt.%; Table 1 and 2) too small for an accurate evaluation of its behavior. Nevertheless, an analogy between the Si–Fe (Fig. 5d) and the C–Fe (Fig. 5a) diagrams can be drawn and suggests a similar behavior for the two elements during the reaction. In conclusion, the microanalyses of the materials inside the microcavities show a random distribution in the C versus O diagram, Fig. 5l. This leads to the conclusion that the presence of oxygen inside these materials is the result of slight oxidation during sample polishing. In contrast, in the same diagram, the material outside the damage mark shows an approximately exponential curvilinear behavior (Fig. 5l) that converges towards the maximum carbon values of the material inside the microcavities, as in the C–Fe diagram of Fig. 5a.

5 Discussion

Cardone et al. suggested that the neutron bursts emitted by the steel and ferrite bars during the ultrasound treatment are either due to piezonuclear reactions induced by energy density sufficient to generate local space-time deformation or to microplasma ignition triggered by a local energy release [10]. Both hypotheses are consistent with the occurrence of microcavities in the bar, which, unlike the ferrite matrix, are incapable of promptly releasing the energy received from the ultrasound waves. The large number of highly deformed cavities inside the sample containing the damage mark (Fig. 3) strongly supports the piezonuclear hypothesis. In fact, their maximum size ($\sim 10 \mu\text{m}$) is consistent with the theoretical calculations of the space-time deformation induced by cavitation [5, 6]. According to these calculations, the power (19 W) of the ultrasound applied to the bar transferred over 370 GeV of energy to the internal cavities guaranteeing their collapse and the triggering of the subsequent piezonuclear reactions [4, 6]. In addition, the presence

of chaotic amorphous materials and/or submicroscopic particles appears to be in agreement with the theory proposed by Nobel Laureate P.W. Bridgman stating that at elevated pressures matter can literally transform into a cloud of subatomic particles [e.g., 18].

Following these hypotheses it is logical to conclude that the external damage characterized by cratering and elements foreign to the ferrite is the product of piezonuclear reactions taking place within empty or gas-filled subsurface micropores (microshrinkage or microporosity) that typically form during metal casting.

On the other hand, the attempts by Ridolfi et al. [11] to hypothesize some other processes that could produce the observed damage and chemical changes have been of little success. For example, the external damage marks could be the result of the combustion of sulfur minerals commonly found in Fe–C alloys, such as the CaS inclusions present in the analyzed bar. However, these inclusions were not found to be in contact with gas (and therefore with the hypothetical oxygen) inside the cavities but rather as occasional single inclusions completely filling the inter-crystalline spaces of the ferrite. In addition, such a combustion process should have left calcium-rich residues and been characterized by the oxidation and partial release of sulfur in the form of a gas during the subsurface microexplosions. This is in contrast with the results of the damage mark analyses. The calcium in the fractured material of the damage mark is found only occasionally (Table 2) while the approximately linear behavior of the sulfur in the S–Fe diagram and its convergence towards the ferrite composition (Fig. 5e) suggests that S should represent a primary element.

Ridolfi et al. [11] also posed the following questions: (I) Why is the amount of structural damage and chemical changes to the bar surface greater than those inside the bar? (II) Why does the carbon content in the microcavities inside the bar appear higher than in the blackish material of the damaged surface? (III) Are these differences the result of more than one reaction mechanism operating in the same bar? (IV) What role do the impurities and inclusions play in the reactions inside and on the surface of the ferrite bar treated with ultrasound?

First, let us consider the latter of these questions (i.e. IV). Specifically, the role of the non-metallic inclusions in light of the gathered semi-quantitative SEM-EDS data. The only inclusions found inside the elongate microcavities having a long dimension of $15 \mu\text{m}$ are Mg–Ca spinels. It is possible that these spinels were also present inside the smaller cavities ($\leq 10 \mu\text{m}$) and have undergone some type of reaction/melting under the influence of the ultrasound. Observing the data in Tables 1 and 2, we can conclude that these inclusions have made minimal to zero contribution as the observed contents of Mg and Ca, which represent the primary components of these crystalline phases [i.e.,

(Mg, Ca)Al₂O₄], are at the EDS detection limit. Despite a thorough investigation of the interiors of the samples, it is not possible to conclude without shadow of a doubt that other inclusion types were not present inside the ferrite bar. Nevertheless, it is highly improbable that such inclusions have contributed to the observed chemical variations. In fact, among the numerous inclusions commonly found in sintered metals [e.g., 14], none has been found to contain chlorine, an element that is consistently present in the cratered bar surface (Table 1) and that shows an inverse variation with iron (Fig. 5f). In addition, at room temperature chlorine is a gas which makes its introduction to the bar surface during fabrication (i.e., casting and hot wire drawing) highly improbable.

The above reasoning assumes that questions (I), (II) and (III) can only be answered using theoretical reasoning. In fact, the results of this work appear to be in direct contrast with the physical laws in flat Minkowski space-time (i.e., where the Lorentz Invariance is strictly valid). However, they can be explained by the theory of the violation of the Local Lorentz Invariance and, specifically, by that of the space-time deformation triggered by a spherically symmetric collapse or by a sudden catastrophic rupture [5, 6, 19]. The reaction products inside the microcavities are most likely the result of spherically symmetric collapse. This collapse has triggered the production of elements such as C, Mn and Cr that show linear variation patterns with iron (Figs. 5a, i, j). In the external damage zones, the spherically symmetric collapse most likely ended with the catastrophic rupture of pore walls thus producing the observed cratering. Therefore, the spherically symmetric collapse is followed by an explosive event characterized by shock wave velocities in excess of those produced by the spherically symmetric collapse itself ($4v_s$, where v_s is the velocity of sound). This is in agreement with the effects of a microscopic violation of the Lorentz Invariance on piezonuclear reactions predicted by Cardone and co-authors [e.g., 4, 6, 19]. As a result, the spherically symmetric collapse-triggered production of carbon on the surface of the bar was followed (or accompanied) by the microexplosion-triggered formation of elements foreign to the ferrite. This hypothesis appears to be in agreement with the observed non-linear (i.e. curvilinear) behavior of carbon and chromium measured in materials within the external cratering (Figs. 5a, i). In addition, the convergence of the linear and curvilinear data distributions in Fig. 5a supports a two-stage piezonuclear process whereby the carbon produced during the symmetrically spherical collapse and iron already present in the matrix are involved in further piezonuclear reactions producing elements foreign to the ferrite (O, S, Cl, K and Cu) via catastrophic explosions. This conclusion is further supported by the chemical changes measured after experiments involving the electric explosion of titanium foil in water [20, 21].

In conclusion, the correspondence of the internal microcavities and the center of the external damage zone along the entire length of the bar suggests that the violation of the Lorentz Invariance during ultrasound treatment only takes place in sections of the bar where the energy build-up per unit time is sufficient to trigger the reactions. Although this assumption requires additional experimental work and further analysis, it is in agreement with the lack of amorphous materials in cavities smaller than 5 μm, and hence of optimal dimensions (i.e., $\leq 10 \mu\text{m}$, see Ref. [19]), inside the ferrite bar not in correspondence with the external damage.

6 Conclusions

The chemical changes induced by ultrasound can be summarized as follows:

- the material in the microcavities shows a systematic increase in carbon (C), chromium (Cr) and manganese (Mn), and decrease in iron (Fe) (Table 1, Fig. 5);
- the surface damage zone shows a systematic increase in carbon (C), oxygen (O), sulfur (S), chlorine (Cl), potassium (K), chromium (Cr) and copper (Cu), and decrease in manganese (Mn) and iron (Fe) (Table 1, Fig. 5).

The elements foreign to the ferrite bar are: O, oxygen; Cl, chlorine; K, potassium; and Cu, copper.

These results are in agreement with the theoretical model predicting the deformation of the space-time and the violation of the Local Lorentz Invariance, and suggest that nuclear reactions characterized by transmutation phenomena and the emission of neutron bursts accompanied by an absence of gamma emissions can occur following the application of mechanical pressure alone.

These piezonuclear reactions appear to take place in two distinct and successive phases (symmetrically spherical collapse and catastrophically explosive rupture). At equal applied pressures, these reactions should depend on the size of the micropores in the ferrite ($\leq 10 \mu\text{m}$) since the amount of energy per unit time accumulated during the symmetrically spherical collapse increases with decreasing pore size (e.g., [6, 19]). The results of the present work did not allow us to determine if these piezonuclear reactions depend on the presence or absence of gases inside the micropores or on the initial micropore geometry. In fact, it seems logical to assume that fabrication of the ferrite bar by hot wire drawing may have produced elongated micropores along its surface due to the stretching of pre-existing micropores or by the simple incorporation of air into its surface as it was drawn through the die.

The careful consideration of the SEM-EDS data gathered during this work has allowed us to reasonably exclude the possibility that the detected elements foreign to the ferrite (particularly chlorine) originated from either inclusions

Table 3 Relationships between the power applied during the ultrasonic experiments and the air, ferrite and water mass to volume densities (D)

Matrix	D (kg/m ³)	D_{air} D_{matrix}	Power (W)	Power $D_{\text{air}}/D_{\text{matrix}}$ (W)
Ferrite	7874	1.5×10^4	19	1.3×10^5
H ₂ O solution	997	1.2×10^3	130	1.1×10^5

See Table 4 for D_{air} value used

common to Fe–C alloys or contamination during wire drawing. However, the theory of piezonuclear-induced transmutation needs to be tested using a variety of isotopic and atomic analytical methodologies. In addition, a large amount of quantitative statistical data is needed to confirm the occurrence of such transmutations after the application of pressure waves to bars of the same composition.

Taking into consideration the current state of the art, it would be inappropriate to propose the occurrence of other piezonuclear reactions (e.g. [10]) also because the proposed two-stage reaction mechanism (spherically symmetrical collapse and microexplosive rupture) needs further evaluation.

7 Final remarks and perspectives

In order to facilitate further investigations and the eventual development of technologic applications (e.g., ultrasound treatments to decrease the radioactivity of nuclear waste; as suggested in [9, 22]), it is useful to summarize the main physical parameters gathered during the ultrasound treatment of the ferrite bar and compare them with those gathered during the experiments with aqueous solutions (e.g., [7, 8]).

Cardone et al. [10] have found a correlation between the power setting, start of neutron emissions and sample density in ultrasound experiments in dilute aqueous solutions and in steel. In light of the possible triggering of piezonuclear reactions by the presence of inter-crystalline micropores in solids and cavitation bubbles in liquids, a comparison of the power setting of the ultrasound machine and the density difference between the treated materials and air (the presence of which in both the cavitation bubbles and the ferrite micropores is likely) was conducted. Table 3 demonstrates that the values obtained by dividing the applied power by the air to matrix (i.e., ferrite or water) density ratio are very similar (1.3×10^5 and 1.1×10^5 , respectively). This suggests that the triggering of piezonuclear reactions by ultrasound treatment of materials with densities higher than that of iron will occur at power settings below the 19 W used in the experiments with steel and ferrite bars.

Table 4 Densities of the microcavity-rich zone in the ferrite bar calculated using a maximum pore diameter of 10 pm

$D_{n/V}$ (m ⁻³)	$D_{n/M}$ (kg ⁻¹)	$D_{v/V}$ –	$D_{m/M}$ –
5×10^{13}	6×10^9	3×10^2	4×10^6

n : number of cavities, v : cavity volume, m : cavity mass, V : ferrite volume, M : ferrite mass. Pore mass was calculated assuming the air density at standard conditions (1.2 kg/m³); the density used for the ferrite matrix is 7874 Kg/m³

In addition, there is an agreement between the distances traveled by the ultrasound waves in the two materials (iron and water) and the start of neutron emissions. By multiplying the speed of sound in iron ($v_s^{\text{ferrite-steel}} = 5800$ m/s) by the time interval between the start of the experiment and the emission of the first neutrons (300 s), a distance traveled by the ultrasound waves was calculated as 1.7×10^6 m. However, taking into consideration that the R-1-S machine generates two sets of ultrasound wave-fronts of opposite direction, which means that the ferrite bar is crossed by the ultrasound two times, the total distance traveled within the ferrite is doubled (i.e., 3.4×10^6 m). This value is very similar to the distance estimated for the experiments in water solutions (i.e. 3.6×10^6 m, calculated for one wave-front traveling with a $v_s^{\text{water}} = 1480$ m/s and a time interval between the start of the experiment and the first neutron emission of 2400 s; [10]).

The different energy densities reached by the materials (Table 3), and thus the different amount of time before the start of the reactions, are a function of the differences in the matrix densities (liquid or solid) crossed by the ultrasound waves and that of the air in the similar-sized bubbles or cavities, respectively [10, 19],

Table 3 lists the estimated parameters for the microcavity-rich zone inside the ferrite bar (i.e., maximum diameter and densities of the pores in the ferrite). The listed densities represent maximum values as they were estimated using the maximum observed pore size (10^{-5} m). The ratio between the cavity and ferrite masses (i.e., $D_{m/M}$) also represents a maximum value as it was calculated assuming the maximum possible density of gas present inside the cavities during their collapse (i.e. that of air at standard conditions).

Acknowledgements The realization of this article was made possible by the support of A. Renzulli, G. Fattorini and A. Rotili. Special thanks go to W. Sala (Startec Ltd. administrator) for supplying the iron bar. We would also like to thank ASP, American Scientific Publishers, for granting permission to reprint Figs. 3 and 4 (from Ref. [11], Ridolfi F., Cardone F., Albertini G. Ultrasonic Damage in Iron, Journal of Advanced Physics, 2013, Vol. 2, 40–44. Copyright© American Scientific Publishers).

References

1. A. Carpinteri, F. Cardone, G. Lacidogna, Strain **45**, 332–339 (2009)
2. F. Cardone, A. Carpinteri, G. Lacidogna, Phys. Lett. A **373**, 4158–4163 (2009)
3. F. Cardone, V. Calbucci, G. Albertini, J. Adv. Phys. **2**, 20–24 (2013)
4. F. Cardone, R. Mignani, A. Petrucci, J. Adv. Phys. **1**, 1–34 (2012)
5. F. Cardone, R. Mignani, *Energy and Geometry* (World Scientific, Singapore, 2004)
6. F. Cardone, R. Mignani, *Deformed Spacetime* (Springer, Berlin, 2007)
7. F. Cardone, G. Cherubini, A. Petrucci, Phys. Lett. A **373**, 862–866 (2009)
8. F. Cardone, G. Cherubini, R. Mignani, W. Perconti, A. Petrucci, F. Rosetto, G. Spera, Ann. Fond. Louis Broglie **34**, 183–207 (2009)
9. F. Cardone, R. Mignani, A. Petrucci, Phys. Lett. A **373**, 1956–1958 (2009)
10. F. Cardone, R. Mignani, M. Monti, A. Petrucci, V. Sala, Mod. Phys. Lett. A **27**(18), 1250102 (2012). doi:[10.1142/S0217732312501027](https://doi.org/10.1142/S0217732312501027)
11. F. Ridolfi, F. Cardone, G. Albertini, J. Adv. Phys. **2**, 40–44 (2013)
12. “Dispositivo e metodo per rilasciare neutroni”, application number MI2010A001263. <http://nuovonucleare.altervista.org/neutronidai-solidi-brevetto>
13. F. Ridolfi, A. Renzulli, R. Macdonald, B.G.J. Upton, Lithos **91**, 373–392 (2006)
14. http://www.kaker.com/inclusions/demo/html/a_index.html
15. K. Kanaya, S. Okayama, J. Phys. D, Appl. Phys. **5**, 43 (1972). doi:[10.1088/0022-3727/5/1/308](https://doi.org/10.1088/0022-3727/5/1/308)
16. C.H. Langmuir, R.D. Vocke Jr., G.N. Hanson, S.R. Hart, Earth Planet. Sci. Lett. **37**, 380–392 (1978)
17. D. Harlov, A. Renzulli, F. Ridolfi, Eur. J. Mineral. **18**, 233–241 (2006)
18. P.W. Bridgman, Phys. Rev. **29**, 188–191 (1927)
19. F. Cardone, R. Mignani, Int. J. Mod. Phys. E **15**, 911–924 (2006)
20. L.I. Urutskoev, V.I. Liksonov, V.G. Tsinoev, Appl. Phys. (Russia) **4**, 83 (2000). Ann. Fond. L. de Broglie. **27**, 701 (2002)
21. V.D. Kuznetsov, G.V. Myshinskii, V.I. Zhemennik, V.I. Arbuzov, in *Proc. 8-th Russ. Conf. on the Cold Transmutation of Nuclei of Chemical Elements*, Moscow (2001), p. 308
22. A.G. Volkovich, A.P. Govorun, A.A. Gulyaev, S.V. Zhukov, V.L. Kuznetsov, A.A. Rukhadze, A.V. Steblevskii, L.I. Urutskoev, Bull. Lebedev Phys. Inst. **8** (2002)